Journal of
Materials Chemistry B

ROYAL SOCIETY
OF CHEMISTRY

PAPER

View Article Online
View Journal | View Issue

Check for updates

Cite this: *J. Mater. Chem. B*, 2022, **10**, 2534

Molecularly-imprinted hydrogel beads *via* self-sacrificing micro-reactors as safe and selective bilirubin adsorbents†

Shiqi Yin,[a] Yinghui Xu,[a] Zhoujun Wang,[a] Zhiwei Wei,[a] Tao Xu,[a] Weifeng Zhao *[a] and Changsheng Zhao *[ab]

Received 30th August 2021,
Accepted 2nd November 2021

DOI: 10.1039/d1tb01895g

rsc.li/materials-b

For patients who are suffering from liver dysfunction or metabolic obstruction, excessive bilirubin (BIL) in their bodies may cause jaundice with irreversible cerebral injury. Traditional exchange transfusion and photodynamic therapy pose a risk of serious adverse reactions or limited curative effects. Therefore, as a generally used treatment, hemoperfusion (HP) purifies patients' blood with solid adsorbents. However, the development of clinical BIL absorbents is greatly impeded by low selectivity and unsatisfactory blood compatibility. Herein, inspired by oviparity, we propose BIL-imprinted poly(acrylic acid-*co*-sodium *p*-styrenesulfonate)–reduced graphene oxide (PAA–SS–rGO@BIL) hydrogel beads as BIL adsorbents *via* self-sacrificing micro-reactors. In the micro-reactors, cross-linked polymerization is achieved and a solidified gel is formed. The received hydrogel beads show outstanding selective adsorption capabilities toward BIL due to the recognition sites, and π–π and hydrophobic interactions. Such hydrogel beads possess superior blood compatibility owing to their bioinspired heparin-mimicking gel structure. Simulated BIL selective adsorption experiments *in vitro* demonstrate that the BIL concentrations in the plasma of a patient with severe jaundice can be restored to a moderate level within 3 hours. Therefore, hydrogel beads offer new options for clinical BIL adsorption.

Introduction

In patients with liver dysfunction or metabolic obstruction, the metabolic system cannot excrete excessive bilirubin (BIL) regularly. The accumulated BIL in their bodies will lead to jaundice with cerebral injury which is not reversible, and even death may occur in the most severe cases.[1–7] As a consequence, it is indispensable to achieve an efficient, quick and safe removal of BIL concentrations in the human body.[8,9] As a typical clinical therapy, blood purification comprises hemodialysis, hemofiltration and hemoperfusion (HP), and HP receives increased attention.[10–14] HP can remove toxins when patients' blood passes through the hemoperfusion apparatus, and HP is effective in the removal of micromolecular toxins, drugs and wastes. Therefore, as a commmonly used therapy, many adsorbents for BIL removal in HP have been developed based on a variety of adsorption mechanisms. Activated carbon, mesoporous silica and amino functionalized polymeric particles are the most frequently used BIL adsorbents.[15–17] However, the development of these adsorbents is impeded by some shortcomings, such as the low selective adsorption capacity and undesirable blood compatibility.[18–20] Moreover, to prevent coagulation *in vitro*, patients need low-molecular-weight heparin or heparin sodium injection in the conventional HP process. An overdose of heparin as an anticoagulant increases the cost of treatment and the risk of thrombocytopenia or hemorrhage.[21–23] Therefore, it is of great significance to increase the selective adsorption ability and hemocompatibility of the adsorbents.

Molecularly imprinted materials have been commonly used in the separation and purification of proteins, since they can offer advantages such as high selectivity and long-term storage stability, which also benefit the adsorption process of adsorbents in blood purification.[24–26] In classical imprinting, the templates are added into the polymerization system and are extracted from the bulk after polymerization, followed by several post-treatment processes to obtain the desired particle size and expose the recognition sites. The molecular imprinting technique shows apparent advantages due to the quick and simple preparation process, and high purity of the obtained materials. However, the traditional imprinted matrix suffers from obvious disadvantages of inefficient combination with target molecules and difficulty in extracting templates.[27–29]

---

[a] *College of Polymer Science and Engineering, State Key Laboratory of Polymer Materials Engineering, Sichuan University, Chengdu 610065, China. E-mail: zhaochsh70@scu.edu.cn*

[b] *College of Chemical Engineering, Sichuan University, Chengdu, 610065, China*

† Electronic supplementary information (ESI) available. See DOI: 10.1039/d1tb01895g

Hydrogel spheres with enormous surface areas are appropriate for column applications in the clinical HP process, which are suitable options to solve the above-mentioned problems.[30–32] However, the typically applied methods for the fabrication of hydrogel spheres need to overcome the problems of harsh solvents and complicated processes; moreover, the diameters of the acquired materials are inadaptable for column operations. To solve these problems, Song *et al.* fabricated hydrogel beads using self-sacrificing micro-reactors, which realize the inner cross-linked polymerization to obtain the gel structure and succeeding automatic redissolution of shell.[33] Therefore, inspired by oviparity, we utilize this bioinspired strategy to fabricate imprinted hydrogel spheres to promote the selective adsorption process with target molecules.

Heparin, a natural sulfated polysaccharide, has aroused extensive attention because of its outstanding blood compatibility.[34–38] Extensive research on heparin-like hydrogels has been done to enhance the blood compatibility of materials. Due to the abundant carboxyl and sulfonated groups with similar bioactivities to heparin, they can inhibit coagulation activity and promote angiogenesis effectively.[39–41] In our previous studies, Deng *et al.* modified polymeric membranes with *p*-styrenesulfonate (SS) to improve the hemocompatibility.[42] Huang *et al.* utilized several heparin-mimicking chitosan with varieties of carboxymethyl and sulfate groups for blood purification.[43] Song *et al.* incorporated sulfonic groups, hydroxyl groups and carboxyl groups within the hydrogel 3D networks to synthesize reinforced anticoagulant hydrogel microspheres which had no effect on the structures of hemocyte and plasma proteins.[44] Sodium *p*-styrenesulfonate (SSS) possesses abundant π–π conjugation structures and sulfonated groups, which provide strong interactions for bilirubin and great blood compatibility. Acrylic acid (AA) possesses abundant carboxyl groups, and PAA possesses good mechanical strength. We anticipate that by utilizing self-sacrificing micro-reactors, BIL imprinted heparin-like hydrogel beads with outstanding blood compatibility can be produced.

Herein, a hydrogel precursor aqueous solution (monomers (AA, SSS)), an initiating agent (ammonium persulfate (APS)), a cross-linking agent (*N*,*N*′-methylene bisacrylamide (MBA)), templates (BIL) and graphene oxide (GO) suspended in deionized (DI) water and a micro-reactor solution (polyethersulfone (PES) dissolved in *N*,*N*′-dimethylacetamide (DMAc)) were prepared first. Then, we dripped the hydrogel precursor aqueous solution into the micro-reactor solution at 70 °C. Based on the liquid–liquid phase separation, the temporary PES protective shells wrapped the hydrogel precursor solution droplets to ensure the completion of the inner polymerization. After that, the PES shell was self-disintegrated and the hydrogel beads were obtained. We introduced GO to ensure that the droplets have suitable viscosity, and utilized the hydrophobicity of reduced GO (rGO) to increase the adsorption capability of hydrogel beads. Therefore, the imprinted hydrogel beads with bioinspired heparin-like structures can remove the BIL through the recognition sites, and π–π and hydrophobic triple-mechanism interactions. To testify the successful synthesis of PAA–SS–rGO@BIL beads, thermogravimetric analysis (TGA), X-ray photoelectron spectroscopy (XPS) and Fourier transform infrared spectroscopy (FTIR) are performed, and their morphologies are observed by scanning electron microscopy (SEM). As blood-contacting materials, the hydrogel beads are also investigated through blood compatibility experiments. Bilirubin adsorption experiments and simulated hemoperfusion experiments *in vitro* are performed to test the BIL adsorption ability of the hydrogel beads.

Experimental

Materials

DMAc was purchased from Chengdu Kelong Chemical Reagent Co. Ltd. PES was purchased from BASF chemical company. The monomers (AA and SSS), cross-linking agent (MBA), initiating agent (APS), templates (BIL), GO (≥96%) and others were all purchased from Aladdin Reagent Co. Ltd. DI water was used freshly throughout the research.

Preparation of hydrogel beads

We used a bioinspired strategy *via* self-sacrificing micro-reactors to produce hydrogel beads. In the first step, we placed 14 g of PES and 86 g of DMAc into a 200 mL glass Petri dish and stirred the mixture vigorously for 2 hours at 40 °C, and then the homogeneous PES micro-reactor solution was received. Second, we prepared the hydrogel precursor solutions of PAA–SS–GO@BIL and PAA–SS–rGO@BIL beads by dissolving the monomers (AA and SSS with a 4 : 1 mass ratio and a total concentration of 60 wt%), cross-linking agent (MBA, 6 wt%), initiating agent (APS, 2.4 wt%), templates (BIL, 3.6 wt%) and GO (6 wt%) in DI water homogeneously. Similarly, the hydrogel precursor solutions of PAA–SS–GO and PAA–SS–rGO beads were prepared using the same method, but without the templates. Third, the PES solution was preheated to 70 °C for 1 hour by placing the glass Petri dish on a self-acting thermostat, then the hydrogel precursor solution was dripped into it using a 0.7 mm-diameter syringe needle, and then the PES protective shells wrapped the droplets immediately by the liquid–liquid phase inversion process, as shown in Fig. 1. After incubating the temporary core@shell droplets in the micro-reactor solution at 70 °C for 20 minutes, the hydrogel beads were formed and the PES shells were re-dissolved. Later on, the hydrogel beads were separated and washed with DMAc and DI water to elute the residual solvent and templates completely. Half of the PAA–SS–GO and PAA–SS–GO@BIL beads were immersed into ascorbic acid solution (100 mg L^{-1}) at 60 °C for 4 hours to obtain the PAA–SS–rGO and PAA–SS–rGO@BIL beads, respectively. The dried hydrogel beads can be kept for over three months.

Characterization of hydrogel beads

A Q500 thermogravimetric analyzer (TG209F1, Netzsch, Germany) was used to obtain the TGA curves from 25 to 900 °C under a nitrogen atmosphere. The XPS spectra were investigated using an X-ray photoelectron spectrometer

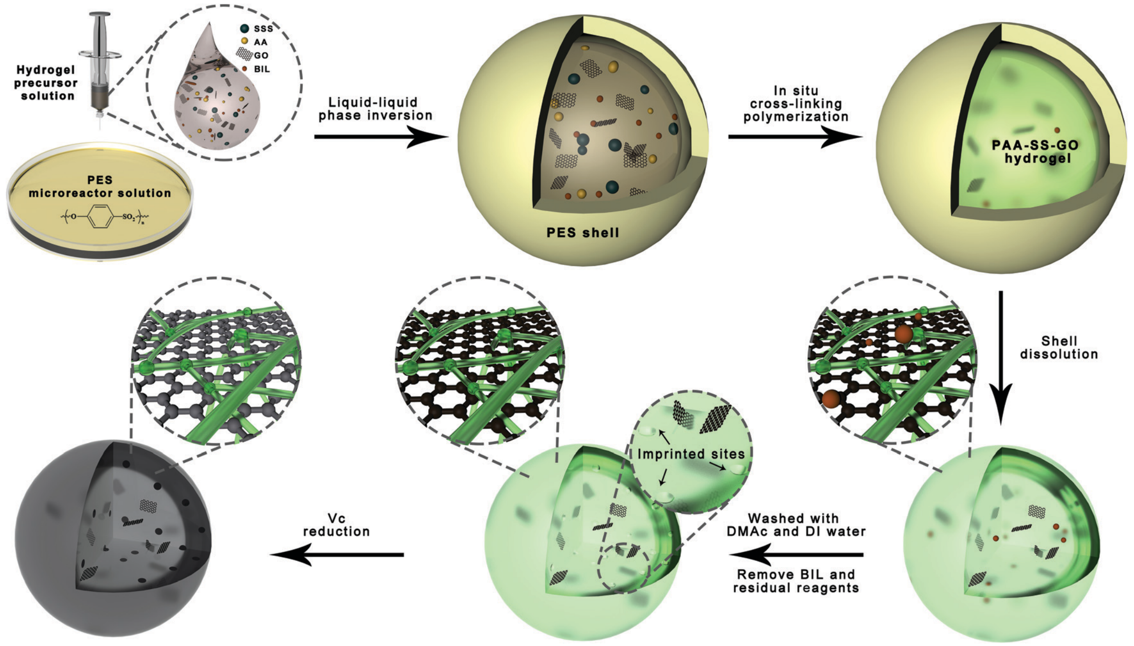

Fig. 1 The schematic illustration of the fabrication of hydrogel beads *via* self-sacrificing micro-reactors.

(Nicolet 560, USA). The chemical structures were obtained from attenuated total reflection FTIR (ATR-FTIR, Nicolet 560) spectra between 600 and 4000 cm^{-1}. A scanning electron microscope (JSM-7610F, JEOL, Japan) was employed to characterize the morphologies on both the surface and cross-section of the hydrogel beads.

The average diameters of the hydrogel beads were calculated using the diameters of at least 6 hydrogel beads which were measured with a rectilinear scale. A universal testing machine (SANS CMT4000, MTS) was employed to investigate the mechanical capacities of the hydrogel beads. To further investigate their mechanical properties, we used a blood pump to make water flow through a syringe needle packed with the PAA–SS–rGO@BIL beads circularly for 60 min, to simulate the flowing pressure in hemoperfusion.

Hemocompatibility experiments

The hemocompatibility of the hydrogel beads was investigated by hemolysis analysis, platelet adhesion, contact activation level, blood routine analysis and clotting time. The detailed procedures are shown in the ESI.†

Bilirubin adsorption experiments

The hydrogel beads (0.01 g) were added into the BIL solutions (dissolved 3 mg of BIL and 40 mg of NaOH into 10 mL of PBS) under oscillation for 2 h. The concentrations of BIL in the solutions before and after adsorption were measured using a UV-vis spectrophotometer (UV-1750, Shimadzu) at 438 nm. All the adsorption experiments were kept in the dark environment, since BILs are easily oxidized into biliverdin by strong light.

Simulated bilirubin selective removal process in HP

To further investigate the practical application of the PAA–SS–rGO@BIL beads as HP absorbents, 0.01 g of the beads were packed into the syringe to simulate the HP process. Restricted to the experimental conditions, the removal ability was tested in simulated plasma instead of whole blood. BILs (340 μg mL^{-1}) (concentration of the patient with severe jaundice) were first dissolved in the plasma (10 mL), and then the plasma was packed into the syringe to investigate the dynamic adsorption process. Uric acid (UA) and creatine (CREA) have a similar structure to BIL. For another group, 340 μg mL^{-1} BIL, 2.05 mg mL^{-1} UA and 3.85 mg mL^{-1} CREA were dissolved in the plasma to discuss the selective adsorption ability of the PAA–SS–rGO@BIL beads.

Results and discussion

Preparation and characterization of PAA–SS–rGO@BIL beads

In this study, the structures of PAA–SS–rGO@BIL beads were well designed, and the bioinspired fabrication process of the beads *via* self-sacrificing micro-reactors is shown in Fig. 1. The actual compositions of the different beads are shown in Table 1.

Table 1 Fabrication and compositions of the PAA–SS–GO, PAA–SS–rGO, PAA–SS–GO@BIL and PAA–SS–rGO@BIL beads

Samples	AA (g)	SSS (g)	GO/rGO (g)	MBA (g)	APS (g)	BIL (g)
PAA–SS–GO/PAA–SS–rGO	4.8	1.2	0.6	0.6	0.24	—
PAA–SS–GO@BIL/PAA–SS–rGO@BIL	4.8	1.2	0.6	0.6	0.24	0.2

As shown in Fig. 1, when the hydrogel precursor solution was dropwise added into the PES solution, a liquid–liquid phase inversion process occurred and the PES protective shells wrapped the droplets immediately because PES was insoluble in water. Then, the polymerization reaction began in the micro-reactors and the polymerization time was shorter than the normal cross-linking polymerization time because of the small volume of the droplets and the high-temperature environment outside. In the polymerization process, the micro-reactors served as the containers of the cross-linking polymerization system and the templates of the droplets in shape. Along with polymerization, the PES shells were re-dissolved in DMAc gradually after the formation of hydrogel beads.

GO was introduced into the hydrogel precursor solution because of its thickening properties, so the droplets could maintain a spherical shape. Furthermore, rGO can enhance the adsorption ability by hydrophobic and π–π interactions. Due to the unsatisfactory blood compatibilities of free GO and rGO, it is feasible to assemble them in the hydrogel structures, so that we can utilize them for BIL adsorption. The introduction of carboxyl contained monomer (AA) and sulfonated group contained monomer (SSS) is a promising way to enhance the blood compatibility; the introduced π–π structure of the functional monomers (SSS) can also enhance the BIL adsorption ability of the hydrogel beads.

The average diameters of the PAA–SS–GO, PAA–SS–rGO, PAA–SS–GO@BIL and PAA–SS–rGO@BIL beads were 2.32, 1.98, 2.38 and 2.36 mm, respectively (Fig. S1, ESI†). The unsmooth surface of the hydrogel beads resulted from the self-sacrificing micro-reactors, which was inevitable and had no effect on the hemocompatibility. As the color change is shown in the figure, the PAA–SS–GO beads showed amber color, and after the reduction or introduction of the templates, the color turned to homogeneous black, preliminarily illustrating the successful fabrication of the PAA–SS–rGO@BIL beads.

As shown in Fig. 2a–d, the TGA, XPS, and FTIR spectra of the PAA–SS–GO, PAA–SS–rGO, PAA–SS–GO@BIL and PAA–SS–rGO@BIL beads were detected to investigate their chemical structures. In the TGA curves, three degradation platforms corresponding to the pyrolysis of residual bound water (0–100 °C), GO/rGO (230–380 °C) and PAA/PSS (405–430 °C) can be observed, respectively. The mass loss of PAA and PSS (≈24 wt%) appeared between 405 and 430 °C; besides, the mass loss of bound water (≈3 wt%) illustrated that the hydrogel beads possess superior hydrophilic properties. In the XPS survey scan spectra, the Na 1s (1072 eV), O 1s (532 eV), S 2s (229 eV) and S 2p (164 eV) signals of the hydrogel beads can be clearly noticed, and the C, N, O, S and Na element contents are summarized in Table 2. The C, N, O, S and Na atom ratios in the PAA–SS–rGO@BIL beads were 70.64, 0.79, 25.53, 2.60, and 0.43 At%, respectively. By estimation, the general contents of the $-SO_3^-$ group (corresponding to the S and Na elements) and $-COO^-$ group in the PAA–SS–rGO@BIL beads were about 0.813 and 6.759 mmol g^{-1}, respectively. In the FTIR spectra, the characteristic peaks of PAA–SS–rGO@BIL emerged at 3450 (corresponding to the –OH group in bound water and –COOH), 2925, 2850 (corresponding to the C–H in $-CH_2-$) and 1190 cm^{-1} (corresponding to the S═O in $-SO_3^-$), respectively, indicating that the sulfo acid group and carboxy group were abundant on the hydrogel bead interfaces. All the above results demonstrated that the PAA–SS–rGO@BIL hydrogel beads had been synthesized successfully.

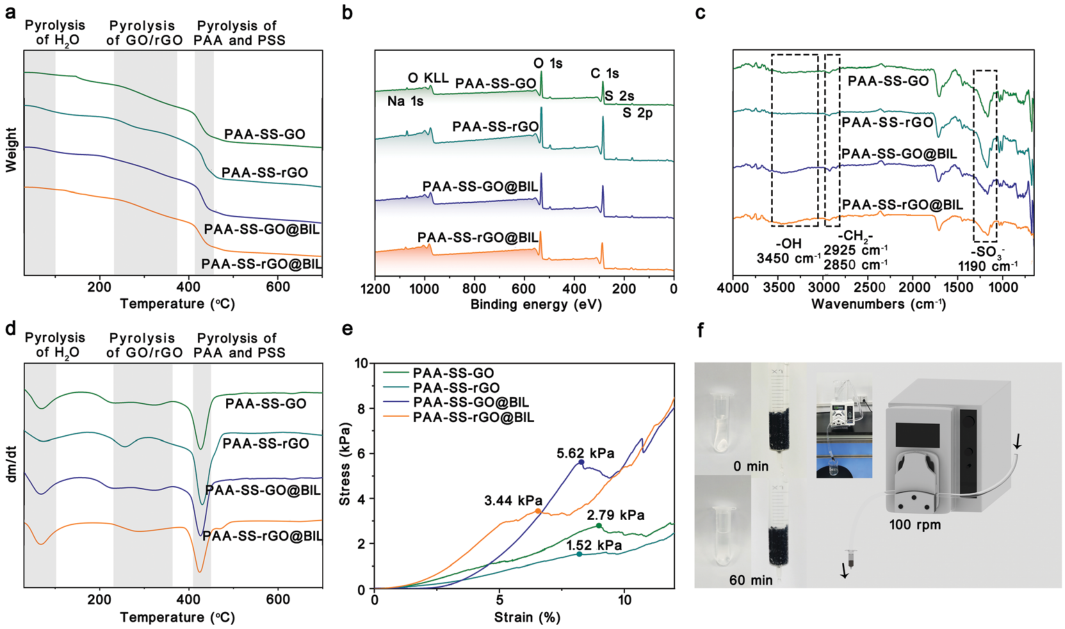

Fig. 2 The TGA curves (a), XPS survey scan spectra (b), FTIR spectra (c), DTG curves (d) and stress–strain curves (e) of the PAA–SS–GO, PAA–SS–rGO, PAA–SS–GO@BIL and PAA–SS–rGO@BIL beads. The characteristic signals are marked and analyzed to certify the successful synthesis of different beads. (f) Digital photographs of the flowing pressure simulation experiment.

Table 2 C, N, O, S, and Na (At%) element contents in different beads

Samples	Element content (At%) C	N	O	S	Na	Estimated $-SO_3^-$ content[a] (mmol g^{-1})	Estimated $-COO^-$ content[a] (mmol g^{-1})
PAA–SS–GO	69.90	1.16	26.43	1.98	0.53	0.619	7.330
PAA–SS–rGO	70.45	0.97	25.34	2.32	0.92	0.725	6.831
PAA–SS–GO@BIL	71.25	0.78	25.52	2.00	0.46	0.625	7.038
PAA–SS–rGO@BIL	70.64	0.79	25.53	2.60	0.43	0.813	6.759

[a] The content of $-SO_3^-$ is calculated using the S peak area, and the content of $-COO^-$ is calculated using the S peak area.

As HP absorbents, good mechanical properties are required to prevent the absorbents from breaking and entering the blood. To further characterize the mechanical properties of the PAA–SS–rGO@BIL beads, as shown in Fig. 2e and f, compression tests were carried out systematically. The stress–strain curves of the PAA–SS–GO, PAA–SS–rGO, PAA–SS–GO@BIL and PAA–SS–rGO@BIL beads were monitored with an electronic universal testing machine. The maximum compressive strengths of PAA–SS–GO, PAA–SS–rGO, PAA–SS–GO@BIL and PAA–SS–rGO@BIL were measured to be 2.79, 1.52, 5.62 and 3.44 kPa corresponding to the first peaks of the curves, respectively. To judge the clinical application of the hydrogel beads objectively, a flowing pressure simulation experiment was employed. DI water in the HP simulating device was clear after 60 min of circulation and no broken beads were observed, which indicated that the PAA–SS–rGO@BIL beads kept the morphology intact during HP for over 60 min.

Morphologies of K-GO/PSS beads

To characterize the morphologies of the prepared hydrogel beads, the hydrogel beads were observed by SEM and the images are shown in Fig. 3. The porous channel structures of the hydrogels were displayed on the surface and inside of the PAA–SS–GO, PAA–SS–rGO, PAA–SS–GO@BIL and PAA–SS–rGO@BIL beads. Furthermore, after adding templates into the hydrogel precursor solution, the diameter of the channel structure showed significant growth, which would improve the removal efficiency of BIL and increase the probability of serving as HP absorbents for the hydrogel beads.

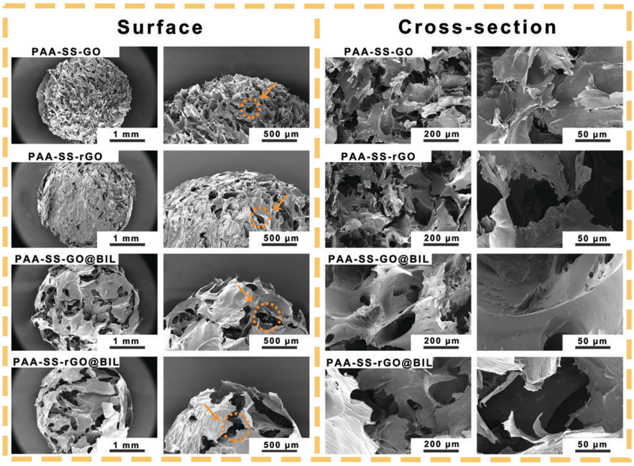

Fig. 3 The representative surface and cross-sectional SEM images of the PAA–SS–GO, PAA–SS–rGO, PAA–SS–GO@BIL and PAA–SS–rGO@BIL beads. The typical gel porous channel structures are marked by orange arrows.

Hemocompatibility of hydrogel beads

To testify the security as HP absorbents, the hemocompatibility of the PAA–SS–rGO@BIL beads was investigated by hemolysis experiment, platelet adhesion experiment, complement activation assay, blood routine examination and clotting time.

Hemolysis index. The red blood cells (RBCs) were incubated with the PAA–SS–GO, PAA–SS–rGO, PAA–SS–GO@BIL and PAA–SS–rGO@BIL beads at 37 °C, respectively, to investigate the hemolysis ratios of the hydrogel beads. After incubating for 3 hours, the representative morphologies of RBCs on the surface of different beads were monitored by SEM, as shown in Fig. 4a. It can be observed that most of the RBCs treated with the hydrogel beads maintained the normal morphologies without damage. As shown in Fig. 4b, the volume distributions of the RBCs incubated with these beads were the same as those of the control group (normal RBCs). Furthermore, as shown in Fig. 4c, we calculated the hemolysis ratios of the hydrogel beads using their absorbances at 540 nm. The hemolysis ratios of the hydrogel beads were lower than 0.4% without exception, which met the requirement of the American Society for Testing Materials standard (5%, ASTM F756-2008). The supernatants of RBCs treated with the hydrogel beads showed transparent separation by centrifugation, illustrating that the RBCs were undamaged. All the above results demonstrated the good RBC compatibility of the PAA–SS–rGO@BIL beads.

Blood routine analysis. To further investigate the hemocompatibility of the PAA–SS–rGO@BIL beads, as shown in Fig. 4d–f, we analyzed the whole blood environment with an auto hematology analyzer (5-diff, BC-5100, Mindray, China). The concentrations of white blood cells (WBCs), RBCs, and PLTs in the blood of the control group and the PAA–SS–rGO@BIL group resulted in very similar values, which revealed that the PAA–SS–rGO@BIL beads had no effect on the entire blood environment. Therefore, such PAA–SS–rGO@BIL beads possessed outstanding hemocompatibility for serving as HP bilirubin absorbents.

Platelet (PLT) adhesion. Adherent and activated PLT can cause serious coagulation and thrombosis.[45,46] The PLT adhesive conditions on the surface of the hydrogel beads were thus investigated as shown in Fig. 5a. The PLTs adhered on the PAA–SS–GO, PAA–SS–rGO, PAA–SS–GO@BIL and PAA–SS–rGO@BIL beads were not activated, which revealed that the advanced hydrophilic properties of the hydrogel beads inhibited the

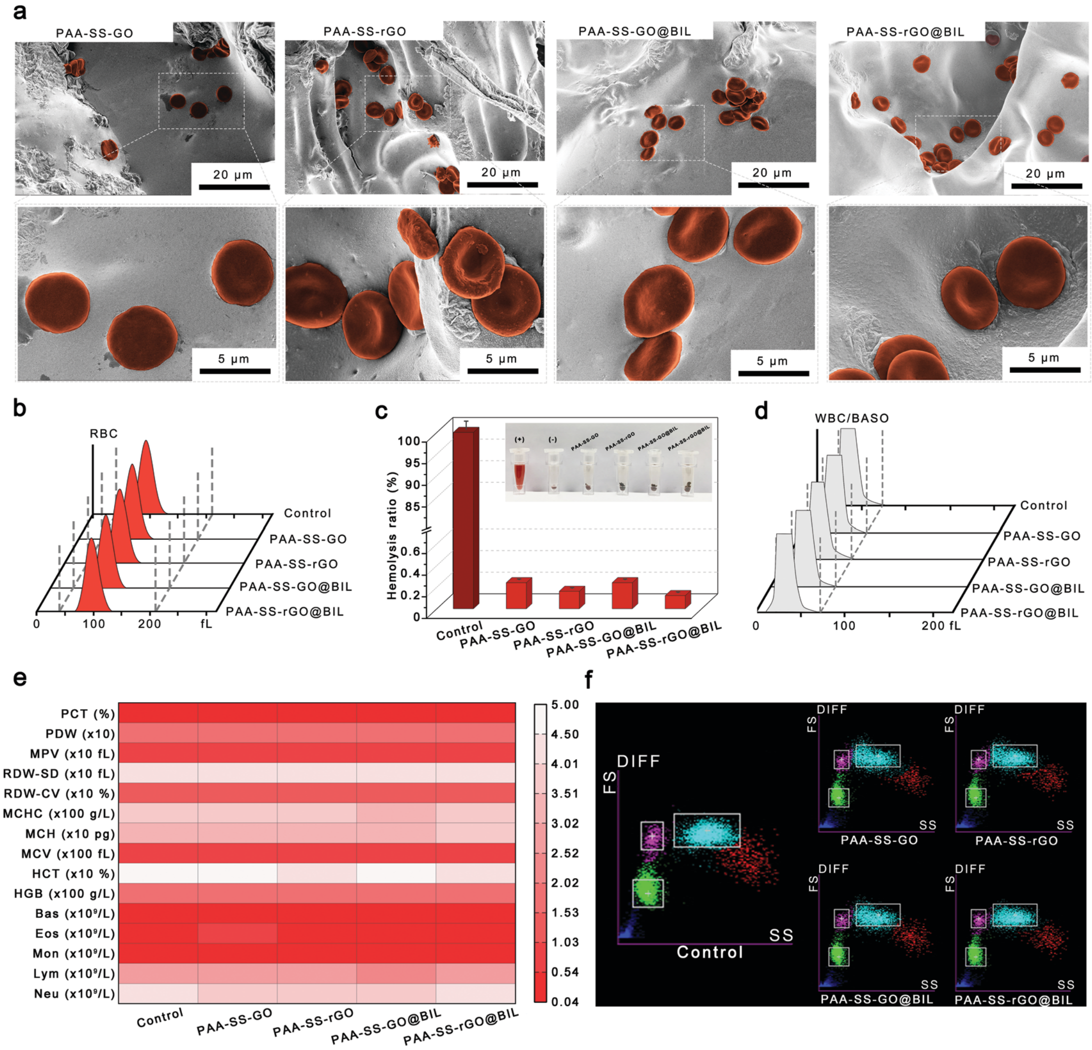

Fig. 4 (a) SEM images of the adhered RBCs on different bead surfaces. The adhered RBCs are marked in red. (b) Volume distribution curves of the control group and the RBCs incubated with the PAA–SS–GO, PAA–SS–rGO, PAA–SS–GO@BIL and PAA–SS–rGO@BIL beads. (c) Hemolysis ratios of the control group, PAA–SS–GO, PAA–SS–rGO, PAA–SS–GO@BIL and PAA–SS–rGO@BIL beads. Inset shows the digital photographs of the '+' and '−' groups and the RBCs incubated with the PAA–SS–GO, PAA–SS–rGO, PAA–SS–GO@BIL and PAA–SS–rGO@BIL beads. The '+' and '−' groups represent the RBCs treated with DI water and saline, respectively. (d) Volume distribution curves of the control group and the WBCs incubated with the PAA–SS–GO, PAA–SS–rGO, PAA–SS–GO@BIL and PAA–SS–rGO@BIL beads. (e) The concentrations of WBCs, RBCs and PLTs in whole blood after incubating with the PAA–SS–GO, PAA–SS–rGO, PAA–SS–GO@BIL and PAA–SS–rGO@BIL beads. (f) The scatter diagrams of differential white blood cell count after incubating with the PAA–SS–GO, PAA–SS–rGO, PAA–SS–GO@BIL and PAA–SS–rGO@BIL beads. Values are expressed as mean ± SD, *n* = 5.

adhesion and activation process of PLTs. As shown in Fig. 5b, the volume distribution curves of PLTs were the evidence of the inhibition effect. The sizes of PLTs in the PAA-SS-GO, PAA-SS-rGO, PAA-SS-GO@BIL and PAA-SS-rGO@BIL groups were similar to those in the control group (normal PLTs), which illustrated that the PLTs were nonactivated. These results indicated the low PLTs' adsorption and activation for the PAA–SS–rGO@BIL beads, and therefore, the potential danger of thrombosis decreased.

Contact activation level. As shown in Fig. 5c and d, the concentrations of platelet factor 4 (PF4) and thrombin–antithrombin (TAT) in blood after incubating with the hydrogel beads were investigated. The TAT concentrations in all the groups were much lower than those in the control group. For the PAA–SS–GO, PAA–SS–rGO and PAA–SS–GO@BIL groups, the concentrations of PF4 in whole blood increased significantly than the control group, while the PF4 concentration in the PAA–SS–rGO@BIL group was slightly higher than that in the control group. All these results revealed the inhibitory effects of the PAA–SS–rGO@BIL beads on PF4 and TAT generation. Furthermore, low hemocompatibility would cause an increase in the Human Complement Fragment 3a (C3a) concentration, and generate allergic toxin reactions.[47,48] As shown in Fig. 5e, to investigate the hemocompatibility of the hydrogel beads, the C3a concentrations in blood after incubating for 1 hour were recorded. Compared to normal blood, the decreasing C3a concentration indicated that the PAA–SS–GO, PAA–SS–rGO, PAA–SS–GO@BIL and PAA–SS–rGO@BIL beads inhibited the

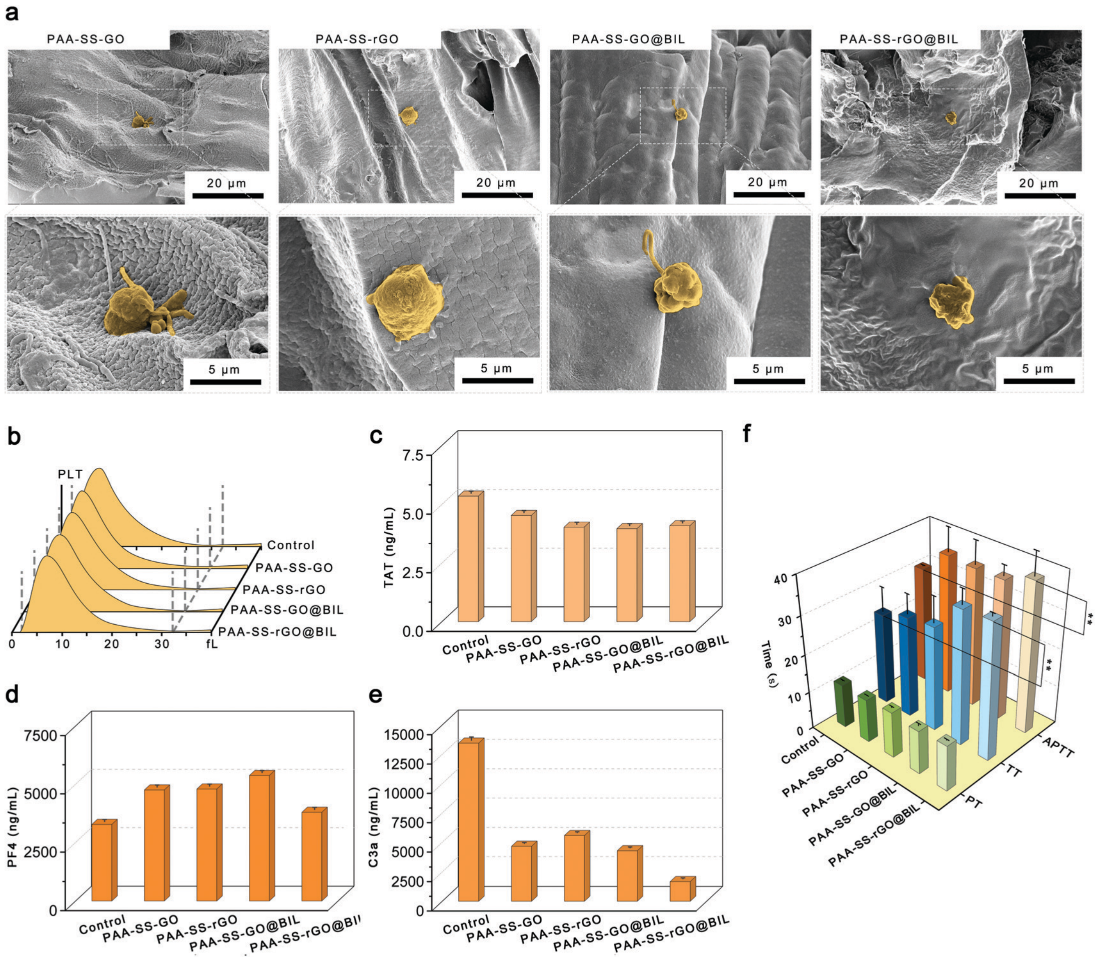

Fig. 5 (a) SEM images of the adhered PLTs on different bead surfaces. The adhered PLTs are marked in yellow. (b) Volume distribution curves of the control group and the PLTs incubated with the PAA–SS–GO, PAA–SS–rGO, PAA–SS–GO@BIL and PAA–SS–rGO@BIL beads. The concentrations of (c) TAT, (d) PF4 and (e) C3a in the whole blood after incubating with the PAA–SS–GO, PAA–SS–rGO, PAA–SS–GO@BIL and PAA–SS–rGO@BIL beads for 1 h. APTT, PT and TT values for the PAA–SS–GO, PAA–SS–rGO, PAA–SS–GO@BIL and PAA–SS–rGO@BIL beads at different dosages. Bare platelet-poor plasma (PPP) is used as a control. Asterisks indicate the significant differences (* $P < 0.05$, ** $P < 0.01$, *** $P < 0.001$). Values are expressed as mean ± SD, $n = 5$.

activation of C3 in blood, and the immunoreaction was inhibited as well. All the results proved that the PAA–SS–rGO@BIL beads possess great hemocompatibility.

Anticoagulant ability of hydrogel beads. The coagulation system consists of intrinsic coagulation pathways (corresponding to the activated partial thromboplastin time (APTT)), extrinsic coagulation pathways (corresponding to the prothrombin time (PT)) and common coagulation pathways (corresponding to the thrombin time (TT)).[49–51] Heparin inhibits the intrinsic and common coagulation pathways, and prolongs the APTT and TT. Therefore, we anticipate that the PAA–SS–rGO@BIL beads with heparin-mimicking functional groups have certain self-anticoagulant capability. APTT, PT, and TT were used to evaluate the anticoagulant abilities of the hydrogel beads, and the results are shown in Fig. 5f. It was concluded that the APTT and TT of the PAA–SS–rGO@BIL beads (39.4 s and 35.6 s) were longer than those of the control group (about 30.8 s and 24.1 s), and their PT values were very similar (about 12.1 s), which demonstrated that the anticoagulation effect of the PAA–SS–rGO@BIL beads with heparin-like functional groups was caused by inhibiting the intrinsic and common pathways. Thus, the PAA–SS–rGO@BIL beads have the potential to decrease the injection dose of heparin in clinics.

Selective bilirubin removal ability of hydrogel beads

As HP absorbents, a single adsorption mechanism always results in low removal efficiency; therefore, the PAA–SS–rGO@BIL beads with triple-model selective adsorption mechanisms were developed to efficiently absorb BIL. As shown in Fig. 6a, on the surfaces of the PAA–SS–rGO@BIL beads, the abundant π–π conjugate structures enhanced the adsorption ability of the hydrogel beads by π–π interactions. Furthermore, the recognition sites and the hydrophobic interaction between rGO and BIL enhanced the combination. The color changes of different beads before and after adsorption are shown in Fig. 6b, and the

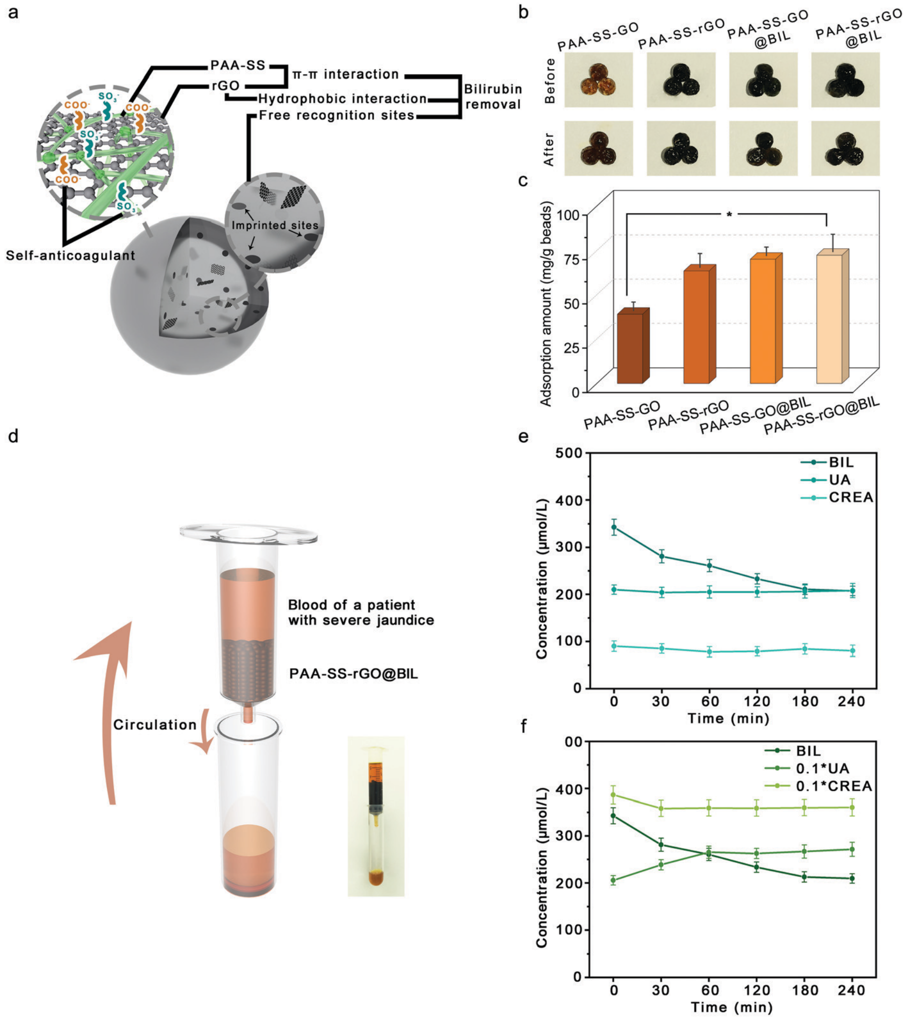

Fig. 6 (a) Schematic diagram of the π–π and hydrophobic interactions and recognition sites between the PAA–SS–rGO@BIL interfaces and BIL. (b) The before and after adsorption digital photographs of the PAA–SS–GO, PAA–SS–rGO, PAA–SS–GO@BIL and PAA–SS–rGO@BIL beads. (c) BIL adsorption amounts of the PAA–SS–GO, PAA–SS–rGO, PAA–SS–GO@BIL and PAA–SS–rGO@BIL beads. Asterisks indicate the significant differences (* $P < 0.05$, ** $P < 0.01$, *** $P < 0.001$). (d) Schematic diagram of the simulated HP process. BIL or BIL/UA/CREA are added to plasma for simulated HP. The inset shows the digital photograph of the simulating device. BIL concentration change curves during HP of the (e) BIL group and (f) BIL/UA/CREA group. All values are expressed as mean ± SD, $n = 5$.

BIL adsorption results were obtained (Fig. 6c). We calculated the BIL adsorbed amounts M(mg g^{-1}) by the following formula:

$$M = (C_0 - C) * V/M_0$$

where C_0 (mg mL^{-1}) and C (mg mL^{-1}) are the BIL concentrations before and after the adsorption process, respectively; V (mL) is the volume of the solution; M_0 (g) is the weight of the dried hydrogel beads. The adsorption amounts of the PAA–SS–rGO@BIL beads (72.38 mg g^{-1}) were higher than those of the other groups, indicating that the adsorption capabilities were enhanced by hydrophobic interactions and recognition sites. The adsorptive properties of the hydrogel beads are theoretically influenced by the contacting time, initial BIL concentration, adsorbent dosage, template dosage and temperature. The removal efficiency of absorbents improved as the contacting time, temperature, adsorbent dosage, template dosage and initial bilirubin concentration increase, but the uptake of all will reach an equilibrium value.[52] The selective adsorption capacity of the PAA–SS–rGO@BIL beads is better than that of the other three.

As shown in Fig. 6d, to further investigate the possibilities for the PAA–SS–rGO@BIL beads as HP BIL absorbents, 0.01 g of the beads were packed into the syringe to simulate the HP process. First, we dissolved 340 μg mL^{-1} BIL (concentration of the patient with severe jaundice) in the plasma; then, we added the plasma (10 mL) into the device to investigate the dynamic adsorption process; for another group of 340 μg mL^{-1} BIL, we added 20.5 mg of uric acid and 38.5 mg of creatine in the plasma additionally to discuss the selective adsorption ability of the PAA–SS–rGO@BIL beads. During the process, the BIL, UA and CREA concentration change curves were detected as shown in Fig. 6e and f. The concentration of BIL can be restored to a moderate level within 3 hours by such a simulated HP process, no matter whether the competitive adsorptions are existing or not.

We introduced a selective coefficient (λ), which is the ratio of the adsorption amounts of BIL to UA or CREA, as follows

$$\lambda_{\mathrm{UA}} = P_{\mathrm{BIL}}/P_{\mathrm{UA}},\ \lambda_{\mathrm{CREA}} = P_{\mathrm{BIL}}/P_{\mathrm{CREA}}$$

where P_{UA} (mg g^{-1}), P_{CREA} and P_{BIL} (mg g^{-1}) are the adsorption amounts of UA, CREA and BIL in the BIL/UA/CREA group, respectively. The data of λ_{UA} and λ_{CREA} in the simulated plasma of a patient with severe jaundice were 238.10 and 7.01, respectively, demonstrating the great selectivity of BIL for the PAA–SS–rGO@BIL beads. Furthermore, the ratio of BIL adsorbed amounts for the BIL group to the BIL/UA/CREA group was $0.9823 \approx 1$, which indicated that the adsorption process of BIL won't be affected by other toxins or wastes.

All these results demonstrated that the PAA–SS–rGO@BIL beads with triple adsorption mechanisms and heparin-like structures had outstanding hemocompatibility and robust BIL selective adsorption capacity; thus, the beads have the potential to serve as HP absorbents.

Conclusions

In summary, we have successfully fabricated BIL-imprinted heparin-like hydrogel beads with triple-model adsorption mechanisms which can be applied as bilirubin absorbents in HP. The PAA–SS–rGO@BIL beads possess homogeneous diameters (2.36 ± 0.44 mm). The bioinspired heparin-like functional groups ensure the low hemolysis ratio (0.2%), low PLT adhesion and inhibition effect of contact activation of the beads, demonstrating the outstanding hemocompatibility of the PAA–SS–rGO@BIL beads. Systematic coagulation tests demonstrate that the clotting time can be prolonged by the hydrogel beads, and the injected dose of heparin can be decreased. Furthermore, the PAA–SS–rGO@BIL beads exhibit superior selective adsorption capabilities of BIL due to their recognition sites, and π–π and hydrophobic triple-mechanism interactions. The simulated BIL removal experiment indicates that the BIL concentrations in the plasma can be restored to a moderate level within 3 hours by such a simulated HP process. Conclusively, the PAA–SS–rGO@BIL beads possess acceptable mechanical strength, outstanding hemocompatibility, and superior selective adsorption capability, which could be used in clinical jaundice treatments.

Author contributions

Shiqi Yin: investigation, formal analysis, visualization, and writing – original draft. Yinghui Xu: resources. Zhoujun Wang: visualization. Zhiwei Wei: methodology. Tao Xu: validation. Weifeng Zhao: conceptualization, project administration, and supervision. Changsheng Zhao: supervision.

Conflicts of interest

The authors declare no conflict of interest regarding the publication of this article.

Acknowledgements

This work was financially sponsored by the National Natural Science Foundation of China (51873115 and 52073190) and the 1.3.5 project for disciplines of excellence, West China Hospital Sichuan University (No. ZYJC21014). Chao He from the College of Polymer Science and Engineering and Yanping Huang from the College of Chemistry and Engineering, Sichuan University, are thanked for their kind support for the SEM analysis.

References

1 J. F. Watchko and C. Tiribelli, *N.* Engl. J. Med., 2013, **369**, 2021–2030.
2 J. F. Watchko, *Clin. Perinatol.*, 2016, **43**, 297.
3 Y. Wang, G. Sheng, T. Shi and X. Cheng, *Biosci. Rep.*, 2020, **40**, BSR20192152.
4 S. M. Shapiro, *Semin. Fetal Neonat. Med.*, 2010, **15**, 157–163.
5 J. D. Ostrow, L. Pascolo, D. Brites and C. Tiribelli, *Trends Mol. Med.*, 2004, **10**, 65–70.
6 T. D. Jr. Hinds and D. E. Stec, *Curr. Hypertens. Rep.*, 2019, **21**, 1–7.
7 L. Guo, L. Zhang, J. Zhang, J. Zhou, Q. He, S. Zeng, X. Cui and J. Shi, *Chem. Commun.*, 2009, 6071–6073.
8 X. Song, T. Xu, L. Yang, Y. Li, Y. Yang, L. Jin, J. Zhang, R. Zhong, S. Sun, W. Zhao and C. Zhao, *Biomacromolecules*, 2020, **21**, 1762–1775.
9 B. R. Mueller, *Carbon*, 2010, **48**, 3607–3615.
10 J. D. King, M. H. Kern and B. G. Jaar, *Clin. J. Am. Soc. Nephrol.*, 2019, **14**, 1408–1415.
11 P. M. Honore, D. De Bels, R. Attou, S. Redant and K. Kashani, *Crit. Care*, 2019, **23**, 1–2.
12 S. Bourcier, P. Hindlet, B. Guidet and A. Dechartres, *Crit. Care Med.*, 2019, **47**, 984–992.
13 E. G. Clark, S. Hiremath, L. McIntyre, R. Wald, G. L. Hundemer and M. Joannidis, *Nat. Rev. Nephrol.*, 2020, **16**, 697–699.
14 P. M. Honore, E. Hoste, Z. Molnar, R. Jacobs, O. Joannes-Boyau, M. L. N. G. Mabrain and L. G. Forni, *Ann. Intensive Care*, 2019, **9**, 1–13.
15 J. Chen, Y. Ma, L. Wang, W. Han, Y. Chai, T. Wang, J. Li and L. Ou, *Carbon*, 2019, **143**, 352–361.
16 Z. Li, X. Huang, K. Wu, Y. Jiao and C. Zhou, *Mater. Sci. Eng., C*, 2020, **106**, 110282.
17 Y. Yang, S. Yin, C. He, X. Wu, J. Yin, J. Zhang, L. Ma, W. Zhao, C. Cheng and C. Zhao, *J. Mater. Chem. B*, 2020, **8**, 1960–1970.
18 R. Zhao, T. Ma, F. Cui, Y. Tian and G. Zhu, *Adv. Sci.*, 2020, **7**, 2001899.
19 J. Chen, Y. D. Ma, L. C. Wang, W. Y. Han, Y. M. Chai, T. T. Wang, J. Li and L. L. Ou, *Carbon*, 2019, **143**, 352–361.

20 R. Zhao, Y. M. Li, X. Li, Y. Z. Li, B. L. Sun, S. Chao and C. Wang, *J. Colloid Interface Sci.*, 2018, **514**, 675–685.

21 M. Marchetti, M. G. Zermatten, D. Bertaggia Calderara, A. Aliotta and L. Alberio, *J. Clin. Med.*, 2021, **10**, 683.

22 K. Krauel, P. Preusse, T. E. Warkentin, C. Trabhardt, S. Brandt, I. Jensch, M. Mandelkow, E. Hammer, S. Hammerschmidt and A. Greinacher, *Blood*, 2019, **133**, 978–989.

23 W. N. Whiteley, H. P. Jr. Adams, P. M. W. Bath, E. Berge, P. M. Sandset, M. Dennis, G. D. Murray, K. S. L. Wong and P. A. G. Sandercock, *Lancet Neurol.*, 2013, **12**, 539–545.

24 K. Yang, S. Li, L. Liu, Y. Chen, W. Zhou, J. Pei, Z. Liang, L. Zhang and Y. Zhang, *Adv. Mater.*, 2019, **31**, 1902048.

25 M. J. Whitcombe, I. Chianella, L. Larcombe, S. A. Piletsky, J. Noble, R. Porter and A. Horgan, *Chem. Soc. Rev.*, 2011, **40**, 1547–1571.

26 S. Li, K. Yang, B. Zhao, X. Li, L. Liu, Y. Chen, L. Zhang and Y. Zhang, *J. Mater. Chem. B*, 2016, **4**, 2739–2739.

27 L. X. Chen, S. F. Xu and J. H. Li, *Chem. Soc. Rev.*, 2011, **40**, 2922–2942.

28 Q. Yang, J. H. Li, X. Y. Wang, H. L. Peng, H. Xiong and L. X. Chen, *Biosens. Bioelectron.*, 2018, **112**, 54–71.

29 C. S. Mahon and D. A. Fulton, *Nat. Chem.*, 2014, **6**, 665–672.

30 N. L. Cuccia, S. Pothineni, B. Wu, J. M. Harper and J. C. Burton, *Proc. Natl. Acad. Sci. U. S. A.*, 2020, **117**, 11247–11256.

31 X. Liu, C. Steiger, S. Lin, G. A. Parada, J. Liu, H. F. Chan, H. Yuk, V. P. Nhi, J. Collins, S. Tamang, G. Traverso and X. Zhao, *Nat. Commun.*, 2019, **10**, 493.

32 C. C. Piras, P. Slavik and D. K. Smith, *Angew. Chem., Int. Ed.*, 2020, **59**, 853–859.

33 X. Song, J. An, C. He, J. Zhou, Y. Xu, H. Ji, L. Yang, J. Yin, W. Zhao and C. Zhao, *J. Mater. Chem. A*, 2019, **7**, 21386–21403.

34 I. Capila and R. J. Linhardt, *Angew. Chem., Int. Ed.*, 2002, **41**, 391–412.

35 T. E. Warkentin, M. N. Levine, J. Hirsh, P. Horsewood, R. S. Roberts, M. Gent and J. G. Kelton, *N. Engl. J. Med.*, 1995, **332**, 1330–1335.

36 J. I. Weitz, *N. Engl. J. Med.*, 1997, **337**, 688–698.

37 S. Valimaki, Q. Liu, L. Schoonen, D. F. M. Vervoort, Nonappa, V. Linko, R. J. M. Nolte, J. C. M. van Hest and M. A. Kostiainen, *J. Mater. Chem. B*, 2021, **9**, 1272–1276.

38 Z. Xiao, B. R. Tappen, M. Ly, W. Zhao, L. P. Canova, H. Guan and R. J. Linhardt, *J. Mater. Chem.*, 2011, **54**, 603–610.

39 L. Ma, C. Cheng, C. He, C. Nie, J. Deng, S. Sun and C. Zhao, *Acs Appl. Mater. Inter.*, 2015, **7**, 26050–26062.

40 Z. Oezyuerek, K. Franke, M. Nitschke, R. Schulze, F. Simon, K. J. Eichhorn, T. Pompe, C. Werner and B. Voit, *Biomaterials*, 2009, **30**, 1026–1035.

41 S. N. Pawar and K. J. Edgar, *Biomaterials*, 2012, **33**, 3279–3305.

42 J. Deng, X. Liu, L. Ma, C. Cheng, W. Shi, C. Nie and C. Zhao, *ACS Appl. Mater. Interfaces*, 2014, **6**, 21603–21614.

43 X. Huang, R. Wang, T. Lu, D. Zhou, W. Zhao, S. Sun and C. Zhao, *Biomacromolecules*, 2016, **17**, 4011–4020.

44 X. Song, H. Ji, Y. Li, Y. Xiong, L. Qiu, R. Zhong, M. Tian, J. N. Kizhakkedathu, B. Su, Q. Wei, W. Zhao and C. Zhao, *Nat. Biomed. Eng.*, 2021, **5**, 1143–1156.

45 L. Yang, L. Han and L. Jia, *ACS Appl. Mater. Interfaces*, 2016, **8**, 26570–26577.

46 P. Wang, J. Liu, X. Luo, P. Xiong, S. Gao, J. Yan, Y. Li, Y. Cheng and T. Xi, *J. Mater. Chem. B*, 2019, **7**, 7314–7325.

47 J. R. Dunkelberger and W. C. Song, *Cell Res.*, 2010, **20**, 34–50.

48 N. P. Gerard and C. Gerard, *Nature*, 1991, **349**, 614–617.

49 M. Levi, C. H. Toh, J. Thachil and H. G. Watson, *Br. J. Haematol.*, 2009, **145**, 24–33.

50 W. C. Lin, T. Y. Liu and M. C. Yang, *Biomaterials*, 2004, **25**, 1947–1957.

51 R. K. Kainthan, J. Janzen, E. Levin, D. V. Devine and D. E. Brooks, *Biomacromolecules*, 2006, **7**, 703–709.

52 M. Guo, J. Wang, C. Wang, P. J. Strong, P. Jiang, Y. S. Ok and H. Wang, *Sci. Total Environ.*, 2019, **682**, 340–347.